INL/EXT-21-63429

NRC Multiphysics Analysis Capability Deployment FY 2021 - Part 3

July 2021

Stefano Terlizzi[2], Cole M. Mueller[1], Guillaume Giudicelli[3], Paolo Balestra[1], Alexander D. Lindsay[3], and Javier Ortensi[2]

[1] *Thermal Fluid Systems Methods and Analysis*
[2] *Reactor Physics Methods and Analysis*
[3] *Computational Frameworks*

INL/EXT-21-63429

NRC Multiphysics Analysis Capability Deployment FY 2021 - Part 3

Stefano Terlizzi[2], Cole M. Mueller[1], Guillaume Giudicelli[3], Paolo Balestra[1], Alexander D. Lindsay[3], and Javier Ortensi[2]

[1]Thermal Fluid Systems Methods and Analysis
[2]Reactor Physics Methods and Analysis
[3]Computational Frameworks

July 2021

Idaho National Laboratory
Nuclear Science and Technology
Idaho Falls, Idaho 83415

http://www.inl.gov

Prepared for the
Office of Nuclear Regulatory Research
U. S. Nuclear Regulatory Commission
Washington, D. C. 20555
Task Order No.: 31310019F0015

Page intentionally left blank

SUMMARY

This report details the progress and activities of Idaho National Laboratory (INL) on the Nuclear Regulatory Commission (NRC) project “Development and Modeling Support for Advanced Non-Light Water Reactors.”

The deliverables completed for this report are:

- Deliverable 1c: the capability to model gas mixtures was added to Pronghorn. A test problem mimicking the conditions achieved in a depressurized loss-of-forced-cooling (DLOFC) event was solved with both RELAP-5 and Pronghorn. Pronghorn employed a finite volume method with the Kurganov-Tadmor discretization. The comparison between the mass fraction spatial profiles computed with RELAP-5 and Pronghorn clearly shows the presence of numerical artifacts (i.e., overly diffusive behavior at low Mach numbers). We confirmed that the problem disappears at higher Mach numbers. We recommend future work on the implementation of a low Mach finite volume formulation to better treat low Mach number problems.

- Deliverable 2a: we demonstrated two approaches to model the radiation/conduction/natural convection heat transfer across a stagnant gas for the PBMR-400 design using Pronghorn. The first approach is based on the net radiation method, which relies on the computation of view factors with the Multiphysics Object-Oriented Simulation Environment (MOOSE) ray tracing capability. The second method is a traditional thermal resistance approach. The test problems include both 2D and 3D geometries. In all cases, the results show very good agreement during a DLOFC transient. This confirms that the faster thermal resistance method produces solutions that are equivalent to the net radiation method for this geometry.

- Deliverable 3d: we demonstrated the use of the advection kernel for the delayed neutron precursor equation in Griffin with a 2D MSFR model. The results appear physical but further verification is recommended. We also recommend the addition of conjugate heat transfer to compute the temperatures and model the thermomechanic behavior of the reflectors and other structures. Significant memory and performance issues were encountered in the 3D axisymmetric model. Future work is recommended in this area.

- Task 8g: this task allows multidimensional MOOSE applications to be coupled to system codes (RELAP-7 and SAM). We implemented a faster multiphysics iteration coupling algorithm, which provides an overall 6× acceleration of the 3D-1D coupling of the core multidimensional fluid flow solver and the 1D primary and secondary loop model.

ACKNOWLEDGEMENTS

The authors would like to acknowledge the support from Sebastian Schunert and Sterling Harper of Idaho National Laboratory. This research made use of the resources of the High Performance Computing Center at Idaho National Laboratory, which is supported by the Office of Nuclear Energy of the U.S. Department of Energy and the Nuclear Science User Facilities under Contract No. DE-AC07-05ID14517.

Page intentionally left blank

CONTENTS

FIGURES

TABLES

ACRONYMS

DLOFC	depressurized loss-of-forced-cooling
DNP	delayed neutron precursor
FVM	finite-volume method
HTRs	high-temperature reactors
INL	Idaho National Laboratory
MOOSE	Multiphysics Object-Oriented Simulation Environment
MSFR	Molten Salt Fast Reactor
MSR	Molten Salt Reactor
NRC	Nuclear Regulatory Commission
RPV	reactor pressure vessel
SOW	statement-of-work

Page intentionally left blank

1. INTRODUCTION

This report details the progress and activities of Idaho National Laboratory (INL) in regard to the Nuclear Regulatory Commission (NRC) project "Development and Modeling Support for Advanced Non-Light Water Reactors."

Table 1 provides a summary of the tasks completed for this report. It matches the deliverable number, statement-of-work task, and (short) description of the deliverable with the relevant section in this report.

Table 1: List of deliverables.

Deliverable Number	SOW Task	Report Section	Description
1c	1c	2	Implement the property relations for gas mixtures so that the air-helium natural circulation phase of a depressurized loss-of-forced-cooling (DLOFC) event can be modeled.
2a	2b	3	Develop a sample problem demonstrating how to model the radiation/conduction/natural convection heat transfer across a stagnant gas gap such as that between the core barrel and the vessel wall in a pebble bed design.
3d	3d	4	Implement the ability to use the local concentration of delayed neutron precursors for the analysis of molten-salt-fueled reactors.
—	8g	5	Acceleration 2D or 3D thermal-fluids coupling with 1D loops.

The tasks completed for this report are:

- Task 1c: the capability to model gas mixtures was added to Pronghorn. A test problem mimicking the conditions achieved in a DLOFC event was solved with both RELAP-5 and Pronghorn. Pronghorn employed a finite volume method with the Kurganov-Tadmor discretization. The comparison between the mass fraction spatial profiles computed with RELAP-5 and Pronghorn clearly shows the presence of numerical artifacts (i.e., overly diffusive behavior at low Mach numbers). We confirmed that the problem disappears at higher Mach numbers. We recommend future work on the implementation of a weakly compressible finite volume formulation to better treat low Mach number problems.

- Task 2b: we demonstrated two approaches to model the radiation/conduction/natural convection heat transfer across a stagnant gas for the PBMR-400 design using Pronghorn. The first approach is based on the net radiation method, which relies on the computation of view factors with the MOOSE ray tracing capability. The second method is a traditional thermal resistance approach. The test problems include both 2D and 3D geometries. The results confirm that the faster thermal resistance method produces solutions that are equivalent to the net radiation method for this geometry.

- Task 3d: we demonstrated the use of the advection kernel for the delayed neutron precursor equation with a 2D MSFR model. The results appear physical but further verification is recommended. We also recommend the addition of a conjugate heat transfer in the future to compute the temperatures and model the thermomechanic behavior of the reflectors and other structures.
- Task 8g: this task allows multidimensional Multiphysics Object-Oriented Simulation Environment (MOOSE) applications to be coupled to system codes (RELAP-7 and SAM). We implemented a faster multiphysics iteration coupling algorithm, which provides an overall $6\times$ acceleration of the 3D-1D coupling of the core multidimensional fluid flow solver and the 1D primary and secondary loop model.

2. GAS-MIXTURES

This chapter is focused on the implementation of the gas-mixture relationships in Pronghorn [4]. The relationships were implemented in the context of Deliverable 1c to enable the modeling and simulation of helium-air natural circulation in a depressurized loss-of-forced-cooling (DLOFC).

The remainder of the chapter is organized as follows. The assumptions and the equations employed within the mixing model are reported in Section 2.1. Implementation details are addressed in Section 2.3, while the problem description and the results are presented in Sections 2.4–2.5, respectively.

2.1 Mixing Model

In this section, the equations for the mixing model are stated for general mixtures of $N + 1$ gas species. Section 2.1.1 reports the assumptions for the mixing model. The equations for molar mass and pressure of the mixture are reported in Section 2.1.2, while Sections 2.1.3-2.1.5 include the equations for specific properties, dynamic viscosity, and thermal conductivity, respectively.

2.1.1 Assumptions

The following assumptions are made to model the gas mixtures:

1. Local thermal equilibrium.
2. Absence of inter-species and intra-species chemical reactions.
3. Negligible inter-atomic forces among gas atoms. This is justified by the high temperature and low pressure in the context of the DLOFC scenario.
4. Each gas in the mixture occupies the entire mixture volume at the temperature T and the partial pressure p_i.

In the remainder of this section, the properties of the mixtures, denoted by the subscript g, are calculated as a function of the properties of the components.

2.1.2 Pressure, mass, moles, molar mass

For the assumptions listed in Section 2.1.1, the Dalton law holds for the mixture:

$$p_g = \sum_{i=0}^{N} p_i, \tag{1}$$

where the partial pressures $\{p_i\}_{i=[0,N]}$ are computed at the temperature of the mixture T and the partial specific volume v_i. Moreover, for assumption 2, the total mass of the mixture, m_g, is equal to the sum of the partial masses, $\{m_i\}_{i=[0,N]}$:

$$m_g = \sum_{i=0}^{N} m_i. \tag{2}$$

Analogously to the total mass, the total number of moles n_g is obtained by summing the partial amounts:

$$n_g = \sum_{i=0}^{N} n_i. \tag{3}$$

If we introduce the mass fraction $y_i = m_i/m_g$, the corresponding molar fraction can be expressed as:

$$x_i = \frac{\text{Moles of species i}}{\text{Total moles}} = \frac{y_i/M_i}{\sum_{i=0}^{N} y_i/M_i}. \tag{4}$$

Finally, the molar mass of the gas mixture can be obtained from the partial molar masses from the following weighted average:

$$\frac{1}{M_g} = \frac{n_g}{m_g} = \sum_{i=0}^{N} \frac{y_i}{M_i}. \tag{5}$$

2.1.3 Specific properties

Let ξ_i denote a specific quantity (i.e., property per unit mass) for the gaseous species i, and Ξ_i the associated total quantity. For assumption 2 and 3:

$$\xi_g = \frac{\Xi_g}{m_g} = \frac{\sum_{i=0}^{N} \Xi_i}{m_g} \tag{6}$$

Introducing the identity $\Xi_i = m_i \xi_i$ and bringing m_g within the summation, Equation 6 can be recast as:

$$\xi_g = \sum_{i=0}^{N} \frac{m_i \xi_i}{m_g} = \sum_{i=0}^{N} y_i \xi_i, \tag{7}$$

where we have used the definition of mass fraction. Equation 2 can be utilized to compute the specific enthalpy of the mixture h_g from the partial enthalpies $\{h_i\}_{[i=0,N]}$:

$$h_g = \sum_{i=0}^{N} y_i h_i. \tag{8}$$

From Equation 8 and Hypothesis 1, we can obtain the equation for the specific heat at a constant pressure $c_{p,g}$:

$$c_{p,g} = \sum_{i=0}^{N} y_i c_{p,i}. \tag{9}$$

An equation analogous to Equation 9 holds for the specific heat at constant volume $c_{v,g}$:

$$c_{v,g} = \sum_{i=0}^{N} y_i c_{v,i}. \tag{10}$$

2.1.4 Dynamic viscosity

The dynamic viscosity can be computed with Wilke's model. It relies on the assumption of weak interaction among gas molecules and reads[5]:

$$\mu_g = \sum_{i=0}^{N} \frac{\mu_i}{1 + \frac{1}{x_i} \sum_{j=1, j\neq i}^{N} x_j \phi_{i,j}}, \tag{11}$$

where the interaction factor $\phi_{i,j}$ is defined as:

$$\phi_{i,j} = \frac{\left(1 + \left(\frac{\mu_i}{\mu_j}\right)^{0.5} \left(\frac{M_j}{M_i}\right)^{0.25}\right)^2}{\frac{4}{\sqrt{2}} \left(1 + \frac{M_i}{M_j}\right)^{0.5}}. \tag{12}$$

The RELAP5/MOD3 manual suggests that this relationship be used to describe the dynamic viscosity of a mixture of gases [6].

2.1.5 Thermal conductivity

The thermal conductivity can be described with Mason and Sexena's analogous method [7]. The RELAP5/MOD3 manual suggests the use of this relationship to describe the thermal conductivity in a mixture of gases [6]. The conductivity of the mixture λ_g is given by the equation:

$$\lambda_g = \sum_{i=0}^{N} \frac{\lambda_i}{\left(1 + \sum_{j=1, j\neq i}^{N} G_{i,j} \frac{x_j}{x_i}\right)}, \tag{13}$$

where the interaction term $G_{i,j}$ is given by:

$$G_{i,j} = \frac{1.065}{2\sqrt{2}} \left(1 + \frac{M_i}{M_j}\right)^{-0.5} \left(1 + \left(\frac{\lambda_i^0}{\lambda_j^0}\right)^{0.5} \left(\frac{M_j}{M_i}\right)^{0.25}\right)^2 . \tag{14}$$

The ratio of frozen thermal conductivities λ_i^0/λ_j^0 is written as:

$$\frac{\lambda_i^0}{\lambda_j^0} = \frac{\mu_i\, M_j}{\mu_j\, M_i}. \tag{15}$$

By substituting 15 into Equation 14, we obtain:

$$G_{i,j} = 1.065 \, \frac{\left(1 + \left(\frac{\mu_i}{\mu_j}\right)^{0.5} \left(\frac{M_j}{M_i}\right)^{0.25}\right)^2}{\frac{4}{\sqrt{2}} \left(1 + \frac{M_i}{M_j}\right)^{0.5}}. \tag{16}$$

2.2 Derivatives of material properties

This section reports the derivatives for the material properties with respect to pressure and temperature. The latter are implemented to correctly calculate the Jacobian matrix required by the numerical methods in MOOSE. The accurate computation of the Jacobian matrix allows to reach quadratic convergence of the numerical solution to the correct solution by using the Newton algorithm.

2.2.1 Specific heat capacity

The isochoric and isobaric specific heat are assumed to be constant with respect to temperature and pressure. This simplification is justified by the high temperature of the mixture in DLOFC scenario. The effect of including the specific heat dependence on temperature and pressure will be considered in future work.

2.2.2 Dynamic viscosity

The derivative of the viscosity with respect to temperature can be obtained by differentiating Equation 11:

$$\frac{\partial \mu_g}{\partial T} = \sum_{i=0}^{N} \left(\frac{\frac{\partial \mu_i}{\partial T}\ F_i - \mu_i \frac{\partial F_i}{\partial T}}{F_i^2} \right). \tag{17}$$

In Equation 17, the factor F_i is defined as:

$$F_i = 1 + \frac{1}{x_i} \sum_{j=0, j\neq i}^{N} x_j \phi_{i,j}. \tag{18}$$

The partial derivative of F_i with respect to T can be computed as:

$$\frac{\partial F_i}{\partial T} = 1 + \frac{1}{x_i} \sum_{j=0, j\neq i}^{N} x_j \frac{\partial \phi_{i,j}}{\partial T}. \tag{19}$$

The derivative of the factor ϕ_{ij} is given by:

$$\frac{\partial \phi_{i,j}}{\partial T} = 2\, \frac{\left(1 + \left(\frac{\mu_i}{\mu_j}\right)^{0.5} \left(\frac{M_j}{M_i}\right)^{0.25}\right)}{\frac{4}{\sqrt{2}}\ \left(1 + \frac{M_i}{M_j}\right)^{0.5}}\ \left(\frac{M_j}{M_i}\right)^{0.25}\ 0.5\ \left(\frac{\mu_i}{\mu_j}\right)^{-0.5}\ \frac{\frac{\partial \mu_i}{\partial T}\mu_j - \frac{\partial \mu_j}{\partial T}\mu_i}{\mu_j^2}, \tag{20}$$

that can be recast as:

$$\frac{\partial \phi_{i,j}}{\partial T} = \frac{\left(1 + \left(\frac{\mu_i}{\mu_j}\right)^{0.5} \left(\frac{M_j}{M_i}\right)^{0.25}\right)}{\frac{4}{\sqrt{2}}\ \left(1 + \frac{M_i}{M_j}\right)^{0.5}\ \left(\frac{M_i}{M_j}\right)^{0.25}\ \left(\frac{\mu_i}{\mu_j}\right)^{0.5}} \frac{\frac{\partial \mu_i}{\partial T}\mu_j - \frac{\partial \mu_j}{\partial T}\mu_i}{\mu_j^2}. \tag{21}$$

Equation 17–21 are valid to describe the derivative with respect to pressure if the change $\partial T \to \partial p$ is performed.

2.2.3 Thermal conductivity

The derivative of the mixture's thermal conductivity is computed similarly to what done for the viscosity. By differentiating Equation 13, the following equation is obtained:

$$\frac{\partial \lambda_g}{\partial T} = \sum_{i=0}^{N} \left(\frac{\frac{\partial \lambda_i}{\partial T}\, H_i - \lambda_i \frac{\partial H_i}{\partial T}}{H_i^2} \right). \tag{22}$$

In Equation 22, the factor H_i is defined as:

$$H_i = 1 + \frac{1}{x_i} \sum_{j=0, j\neq i}^{N} x_j G_{i,j}, \tag{23}$$

and its derivative is:

$$\frac{\partial H_i}{\partial T} = 1 + \frac{1}{x_i} \sum_{j=0, j\neq i}^{N} x_j \frac{\partial G_{i,j}}{\partial T}. \tag{24}$$

Noticing that $G_{ij} = 1.065\phi_{ij}$ leads to the following relation:

$$\frac{\partial G_{i,j}}{\partial T} = 1.065\, \frac{\partial \phi_{i,j}}{\partial T}, \tag{25}$$

where $\frac{\partial \phi_{i,j}}{\partial T}$ is defined as in Equation 21. Equation 22–25 are valid for pressure by substituting ∂T with ∂p.

2.3 Implementation

The main part of the implementation is a fluid property object providing an interface that allows the computation of fluid properties given temperature, pressure, and mass fractions. This interface is used by MOOSE material, kernel, and boundary conditions objects by passing the values of pressure, temperature, and mass fractions computed during the iterative solve on each quadrature point. The implemented objects are based upon the current finite volume Pronghorn capabilities and their current application was restricted to binary mixtures. This can be easily extended in the future.

What follows is a description of the objects implemented in the context of this task [8].

GasMixPHFluidProperties – This object implements the relations for fluid properties described in Section 2.1 and provides an interface for on-demand computation of these properties to the MOOSE system.

GasMixPorousMixedVarMaterial – This object duplicates `PorousMixedVarMaterial` for gas mixtures and computes quantities necessary for feeding the `GasMixPHFluidProperties` computation.

GasMixPCNSFVKT – This object duplicates `PCNSFVKT` for gas mixtures. The latter implements the Kurganov-Tadmor discretization scheme for the advection term [9]. Different slope limiters are available to mitigate spurious numerical oscillations and mitigate the numerical diffusivity (e.g., upwind and minmod slope limiters) [10].

GasMixPCNSFVStrongBC – This object duplicates `PCNSFVStrongBC` for gas mixtures and weakly imposes Dirichlet information for fluid temperature, superficial velocity or momentum, pressure, and/or mass fraction(s).

2.4 Problem Description

An isothermal, 10-m high vertical pipe with a flow area of 1 m^2 and porosity of 50% is used to test the new gas mixture capabilities. At time $t = 0^+$, air enters the helium-filled pipe from the top boundary at 0.1 m/s. The problem was defined to recreate the physical conditions of a DLOFC event with minimum computational effort.

The following equation is used to transport the air mass fraction in the pipe:

$$\epsilon \frac{\partial \left(\rho y_a\right)}{\partial t} + \nabla \cdot \left(\epsilon \rho y_a \vec{v}\right) = 0, \tag{26}$$

where:

- ϵ is the porosity,
- ρ is the mixture density,
- y_a is the mass fraction,
- $\vec{v}$ is the velocity field.

The air is modeled as an ideal gas with a heat capacity ratio of 1.4 and molar mass of 29 g/mol. The heat conductivity and viscosity are set to 25.68×10^{-3}W/m/K and 18.23×10^{-6}Pa $\cdot$ s, respectively.

The mass conservation for the porous medium is written as:

$$\epsilon \frac{\partial \rho}{\partial t} + \nabla \cdot (\epsilon \rho \vec{v}) = 0, \tag{27}$$

while the momentum equation for the component i of the velocity is:

$$\epsilon \frac{\partial \rho v_i}{\partial t} + \nabla \cdot (\epsilon \rho \vec{v} v_i) + \epsilon \left(\nabla p\right)_i - \epsilon \rho \vec{g}_i = 0, \tag{28}$$

where $\vec{g}$ is the gravity acceleration. The temperature is set to $T = 523K$. Table 1 reports the inlet and outlet conditions for the problem.

Table 2: Inlet and outlet boundary conditions.

Variable	Inlet/Outlet	Value
y_a	inlet	0.999
v_x, m/s	inlet	0.0
v_y, m/s	inlet	0.1
p, Pa	outlet	7.0e7

2.5 Results and Discussion

The problem described in Section 2.4 is solved by imposing axial symmetry and by discretizing the pipe into 50 equally-high axial cells. The time increment is set to 1 second, and the transient is run for 200 seconds. The value of the helium mass fraction calculated with RELAP-5 [11] for the top, bottom, and middle axial cell as a function of time are reported in Figure 1. In all cases, the helium mass fraction decreases from 1 to 0 due to the air flow entering the pipe. For the middle and bottom element, a time-delay (i.e., a plateau) can be noted before the mass fraction starts decreasing to zero. This is caused by the finite speed of propagation of the mass fraction wave front.

The same problem was solved by leveraging the Pronghorn objects listed in Section 2.3. Figure 2 reports the helium mass fraction in the bottom axial cell calculated using the Kurganov-Tadmor method with the upwind slope limiter. From Figure 2 it can be observed that, despite reaching the correct steady-state solution, (i.e., the helium mass fraction reaches zero), the time-delay observed in Figure 1 is not correctly reproduced. This is because the Kurganov-Tadmor discretization

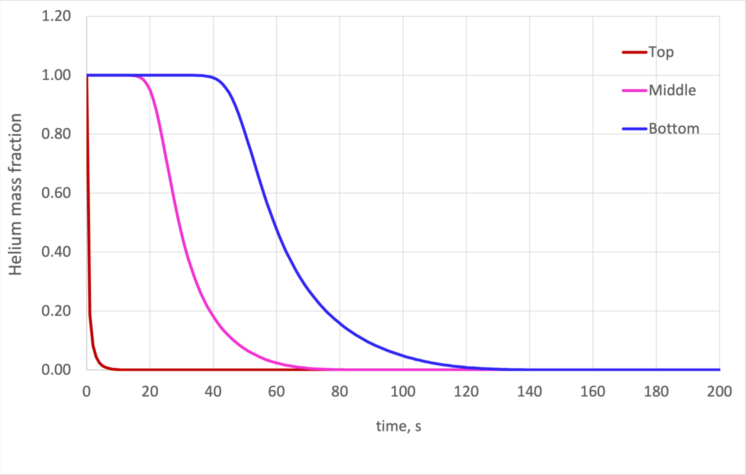

Figure 1: RELAP-5 solution. Helium mass fraction as a function of time for the top, bottom, and middle axial cell.

scheme is highly diffusive at low Mach numbers. Figure 3 shows the spatial distribution of the mass fraction at 25.3 seconds from which it is clear the absence of a clear wave-front. Similar spatial shapes can be observed for the other time steps.

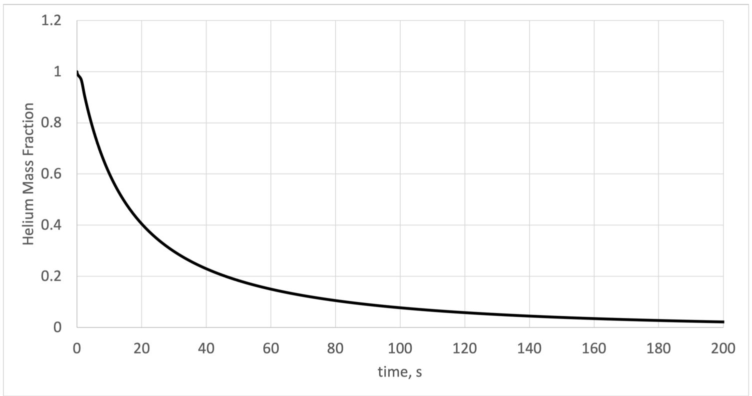

Figure 2: Pronghorn solution with upwind slope limiter for the bottom axial cell. The curves for the top and middle axial cell are not reported because not distinguishable from the one for the bottom axial cell.

Enhanced accuracy can be obtained by resorting to the minmod slope limiter. Figure 4 reports the helium mass fraction as a function of time for the three axial cells of interest. From Figure 4, it is noticeable a less diffusive solution despite the presence of a spurious change of slope at around 25 seconds. A caveat on the use of the minmod slope limiter is that it imposes a much smaller time step, leading in turn to a tenfold increase in computational time with respect to the results obtained with the upwind slope limiter. No improvement in the quality of the results was found

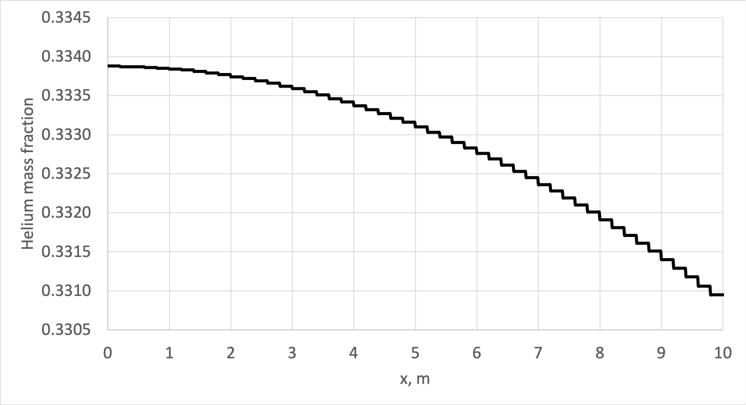

Figure 3: Mass fraction as a function of space at time 25.3 seconds.

by refining the mesh.

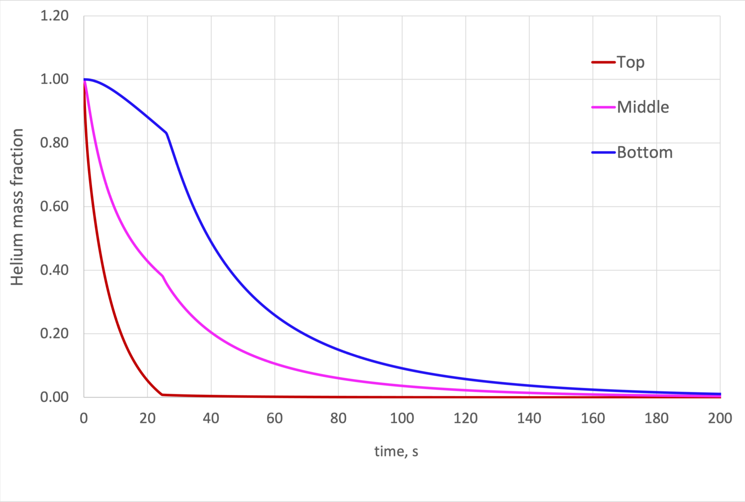

Figure 4: Pronghorn solution with minmod slope limiter. Helium mass fraction as a function of time for the top, bottom, and middle axial cell.

To confirm our hypothesis on the cause of the overly diffusive behavior of the solution, (i.e., the use of the Kurganov-Tadmor discretization scheme with a weakly compressible flow) the problem described in Section 2.4 was run by increasing the inlet speed and reactor dimensions by a factor of 100 to achieve higher Mach numbers. Figure 5 shows the helium mass fraction as a function of time for the top, bottom, and middle axial cell, while Figure 6 reports the air mass fraction's spatial profile at different time steps. From these two figures, a propagation front is clearly visible, therefore confirming the limitations of the currently implemented Kurganov-Tadmor method in dealing with weakly compressible flows characterized by low Mach number.

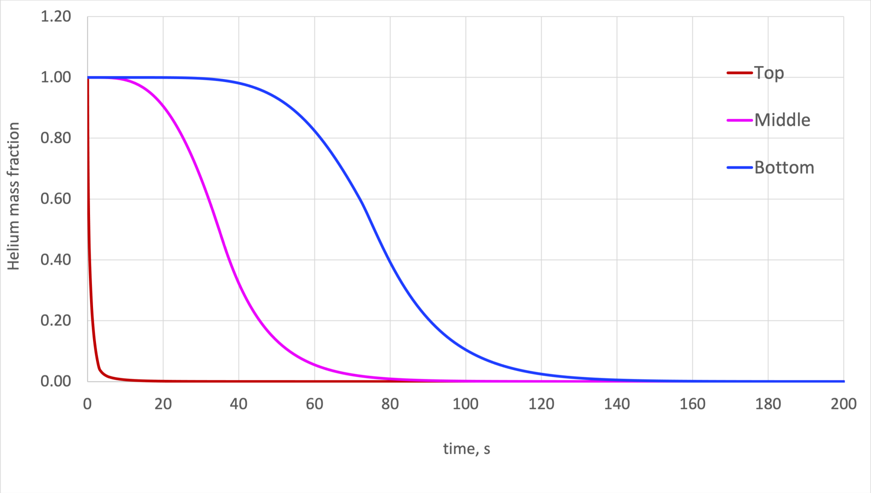

Figure 5: Pronghorn solution with minmod slope limiter and increased Mach number. Helium mass fraction as a function of time for the top, bottom, and middle axial cell.

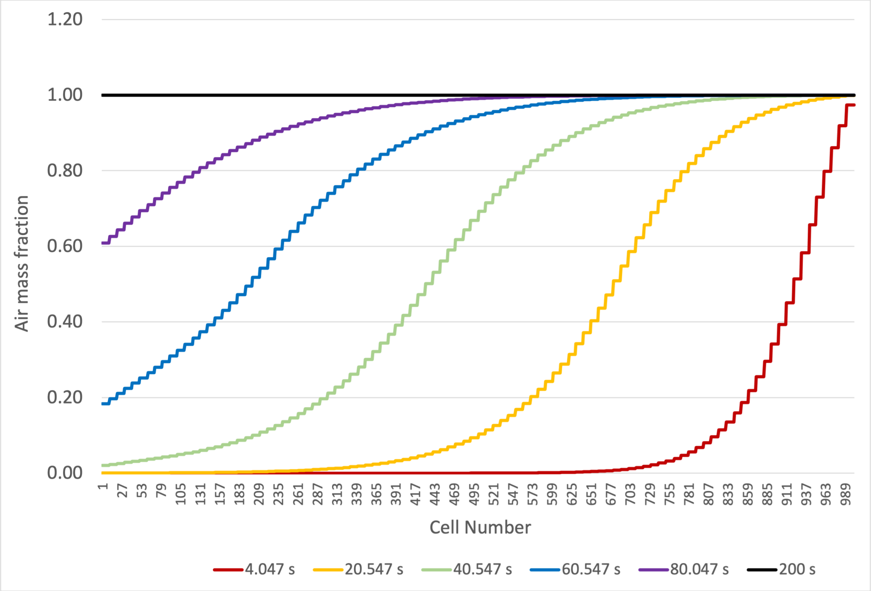

Figure 6: Snapshots of the air mass fraction spatial profile at different times t (in seconds) for increased Mach number.

3. HEAT TRANSFER IN STAGNANT GAPS

There are a number of gap heat transfer models available in BlueCRAB through the MOOSE physics modules. The primary goal of this section is to verify that these gap heat transfer capabilities provide an accurate representation of the physics that take place in a gap with a stagnant gas. This situation is applicable to multiple reactor types including high-temperature reactors (HTRs) and microreactors. An example of the gas gap between the core barrel and the reactor pressure vessel (RPV) is shown in Figure 7.

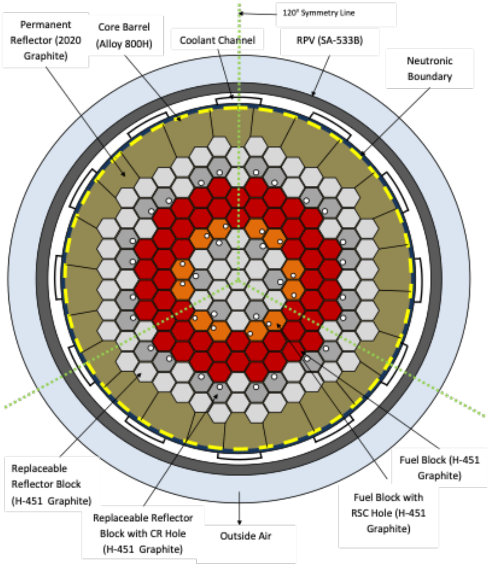

Figure 7: Stagnant gas gap in the MHTGR-350 [1, 2] between the core barrel and reactor pressure vessel.

3.1 Methodology

The dominant heat transfer physics in a gap filled with a stagnant gas are molecular conduction and radiation heat transfer. The convective heat transfer is usually negligible for small gap widths. For example, the helium gap between the reflector and barrel with a surface temperature of 870 K and a bulk fluid temperate of 760 K exhibits a Grashof number of 68.3, Prandtl number of 0.65, and Rayleigh number of 44 [12]. A similar set of dimensionless parameters can be obtained between the barrel and the reactor pressure vessel. The Grashof number is 301.173, with a Prandtl number of 0.65, that results in a Rayleigh number of 196.89. As a reference, turbulent Rayleigh numbers occur near 10^9.

The modeling approaches for gap heat transfer in MOOSE include:

- *Net Radiation Method*. This method simulates radiation as mono-energetic rays and takes absorption and re-emission into account using a single emissivity parameter. Furthermore, it assumes that there is no attenuation in the medium between the surfaces. A MOOSE ray-tracing algorithm is deployed to compute view factors for a number of surface patches defined by the user. The current approach in MOOSE is to use both conduction and the gray diffuse radiative heat transfer models across the gap. In this method, the gap is explicitly meshed.

- *Thermal Resistance Method*. This method employs an electric circuit analog to represent the heat transfer across the gap. The ”thermalContact” action in MOOSE computes the equivalent gap heat transfer without the need for a mesh. In this method, the heat flux is computed and applied as an integrated boundary condition at the quadrature points on both faces. A nearest-node algorithm is used to connect the various interacting points on the surfaces involved. The gap geometry must be specified to apply the appropriate geometry correction (i.e., plate, cylinder, or sphere). This approach allows less memory to be used and eliminates the ray tracing portion of the calculation, thus improving computational speed.

3.2 Problem Description

The test problem selected is based on the modeling of the PBMR-400 [13]. The simplified geometry is a quarter core symmetric section limited to the reflector, core barrel, and RPV but retains the same dimensions as the original benchmark. Three modeling approaches are analyzed:

1. 3D *Net Radiation Method* - this is an azimuthally symmetric model that serves as the reference solution to establish the accuracy of the other two solutions,

2. 3D *Thermal Resistance Method* - this is the 3D analog of the reference model with the faster method, and

3. 2D R-Z *Thermal Resistance Method* - this is the 2D analog of the reference model.

The mesh for Model 2 is shown in Figure 8. In this instance, the gap regions are not meshed. In all three models, heat conduction kernels are used in the solid materials with the particular gap model in the two gap regions bounded by the reflector and barrel (Gap 1) and the barrel and RPV (Gap 2). The problem is azimuthally symmetric to ensure that the 3D solutions are equivalent to the 2D R-Z analog. The boundary conditions for the model are included in Table 3. A time-dependent and z-dependent Dirichlet B.C. is imposed on the inner boundary of the reflector to simulate the core heat source. These values are obtained from the results of a DLOFC using the INL PBMR-400 model [14]. The outer boundary is a radiative heat rejection condition between two concentric, infinite cylinders. This boundary condition computes the radiative heat flux from the boundary to an infinite cylinder completely surrounding it. The top and bottom of the geometry use adiabatic conditions.

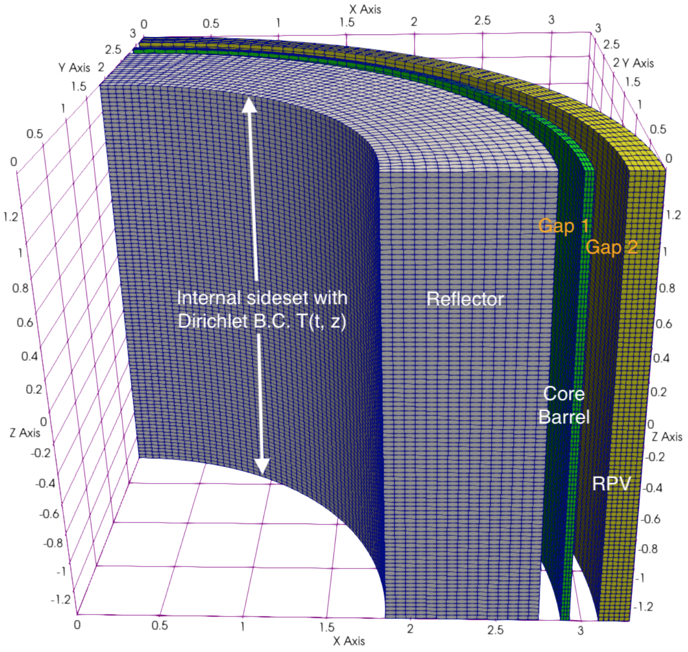

Figure 8: PBMR-400 3D mesh with two gaps. $1/4^{th}$ axial scale (in meters).

The various materials and thermo-physical properties used in the simulations are included in Table 4. Note that the thermo-physical properties are not temperature dependent to simplify the calculations. The radiation heat transfer parameters for Model 1 are shown in Table 5.

Table 3: Boundary conditions for the gap heat transfer model.

Region	Boundary Condition
Reflector inner	Dirichlet with value T(t,z)
RPV outer	Radiative heat transfer between two concentric, infinite cylinders Boundary radius = 4.62 m, $T_\infty = 293.15$ K
Top and bottom	Adiabatic (Neumann B.C.), heat flux value = 0 W/m^2

Table 4: Thermo-physical properties of the various materials and regions.

Material	Region	Density $[\frac{kg}{m^3}]$	Heat Capacity $[\frac{J}{kg-K}]$	Conductivity $[\frac{W}{m-K}]$
Graphite	Reflector	1780	1.697	26
Steel	Core barrel & RPV	7800	0.525	17

3.3 Results and Discussion

A comparison of the problem size is shown in Table 6. We differentiate between the primal variable (temperature) and the auxiliary variables used in the thermal resistance and the net radiation heat transfer algorithms.

The time evolution of the reference solution can be found in Figure 9. The times correspond approximately to 0, 7, 14, 21, 28, 36, 43, and 50 hours. The results show the change in the axial temperature distribution as the forced flow though the core comes to a stop. The reflector and metallic structures heat up during the transient as heat is slowly removed from the core to the ultimate heat sink. A comparison between the reference (Model 1) and the 3D thermal resistance method (Model 2) at various times is included in Figure 10. The results show very good agreement between the two approaches with maximum differences within 3.1 K during the duration of the transient. This confirms that the faster thermal resistance method produces solutions that are equivalent to the net radiation method for this geometry. Another comparison between the reference (Model 1) and the 2D R-Z thermal resistance method (Model 3) at various times is included in Figure 11. Here again, the results show excellent agreement between the two approaches with maximum differences within 3.2 K during the duration of the transient.

Table 5: Radiation heat transfer parameters. The number of directions are per quadrature point.

Region	Emissivity	Directions	Number of Patches
Reflector	0.8	512	100
Core barrel	0.8	512	100
RPV	0.8	512	100

Table 6: Comparison of the problem size.

Model	Primal DoF	Auxiliary DoF
1	212,400	401,940
2	159,300	275,616
3	1,768	2,884

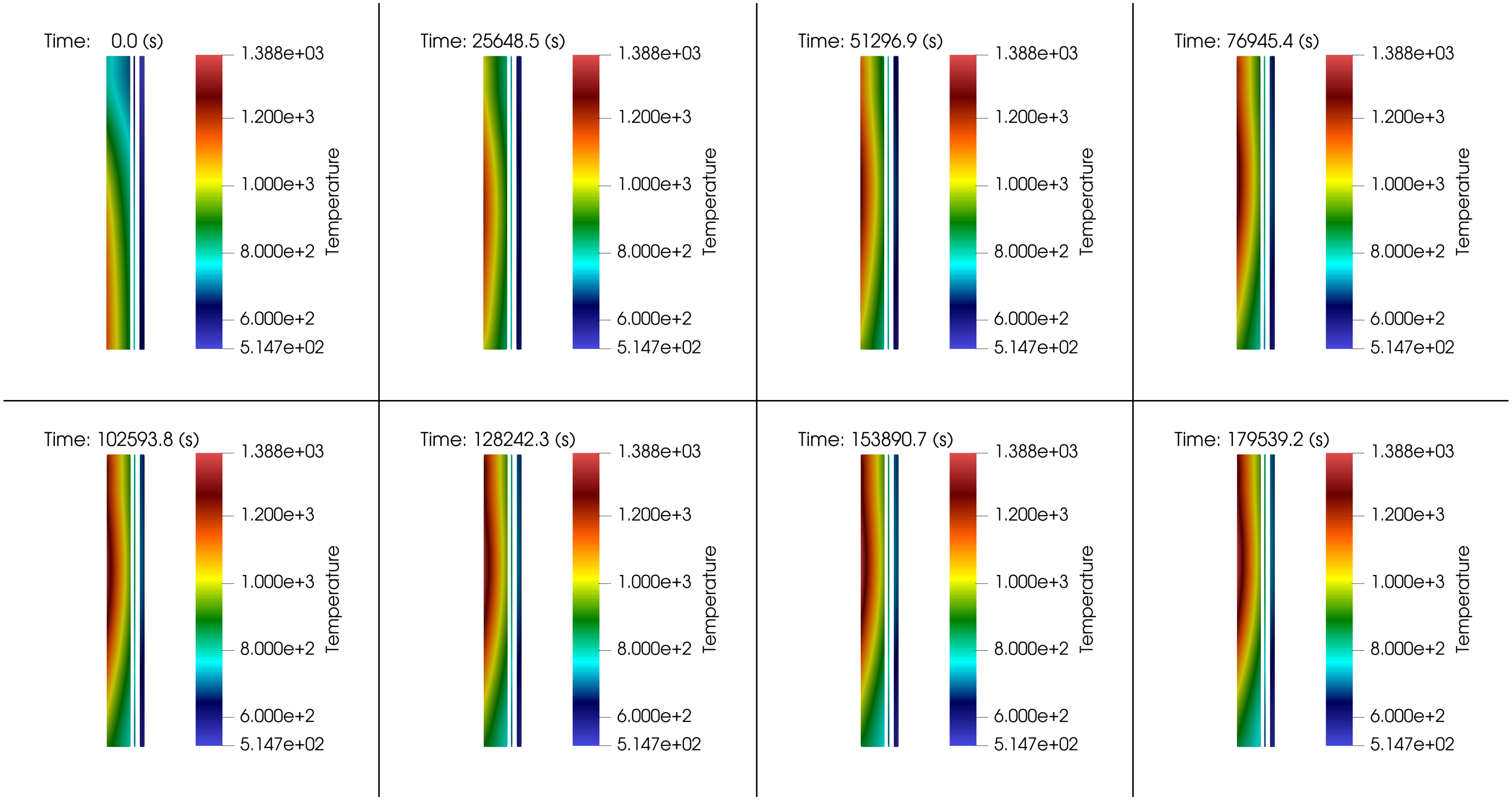

Figure 9: Reference solution from the 3D net radiation method.

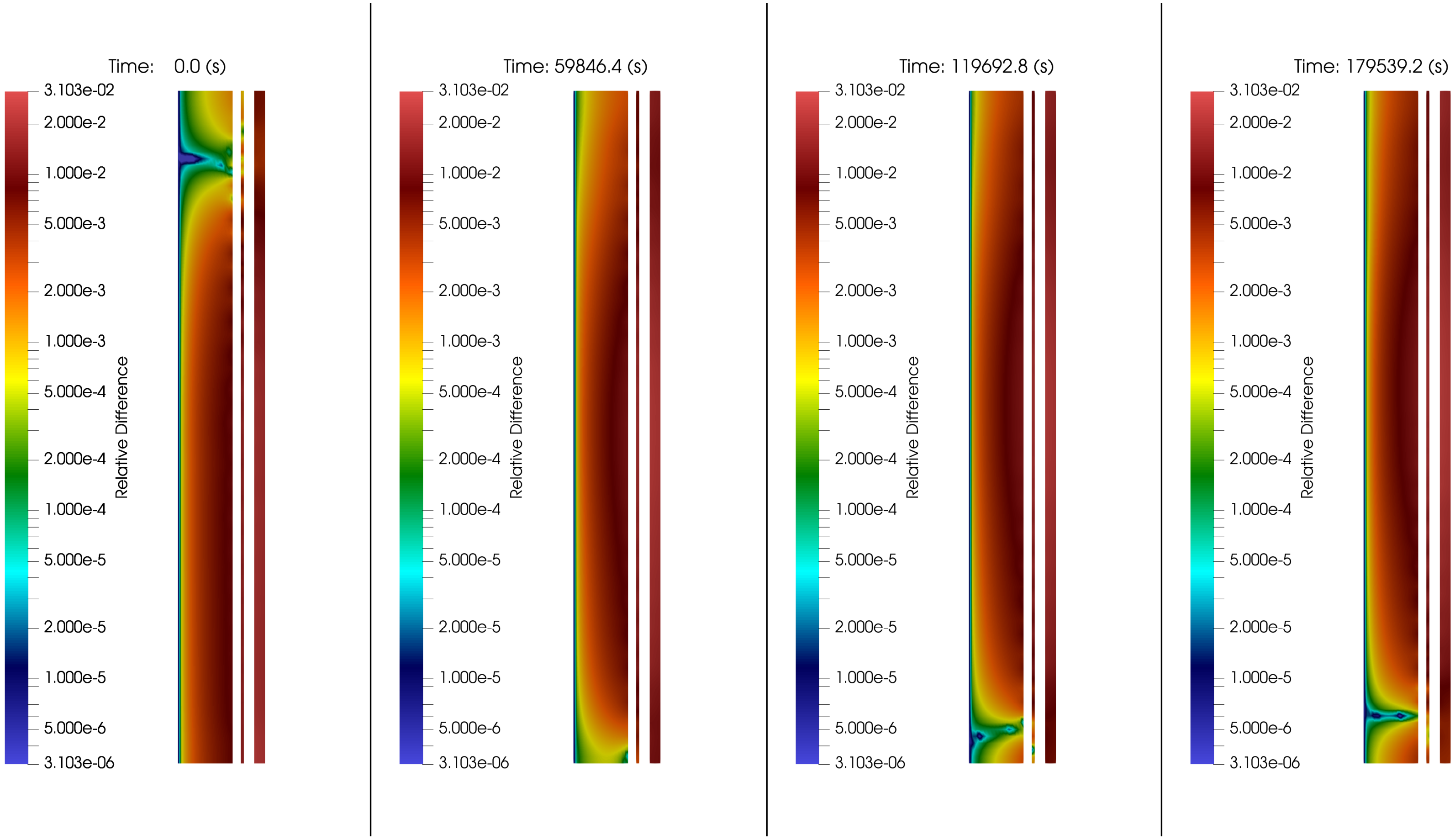

Figure 10: Comparison of 3D net radiation method and 3D thermal resistance method.

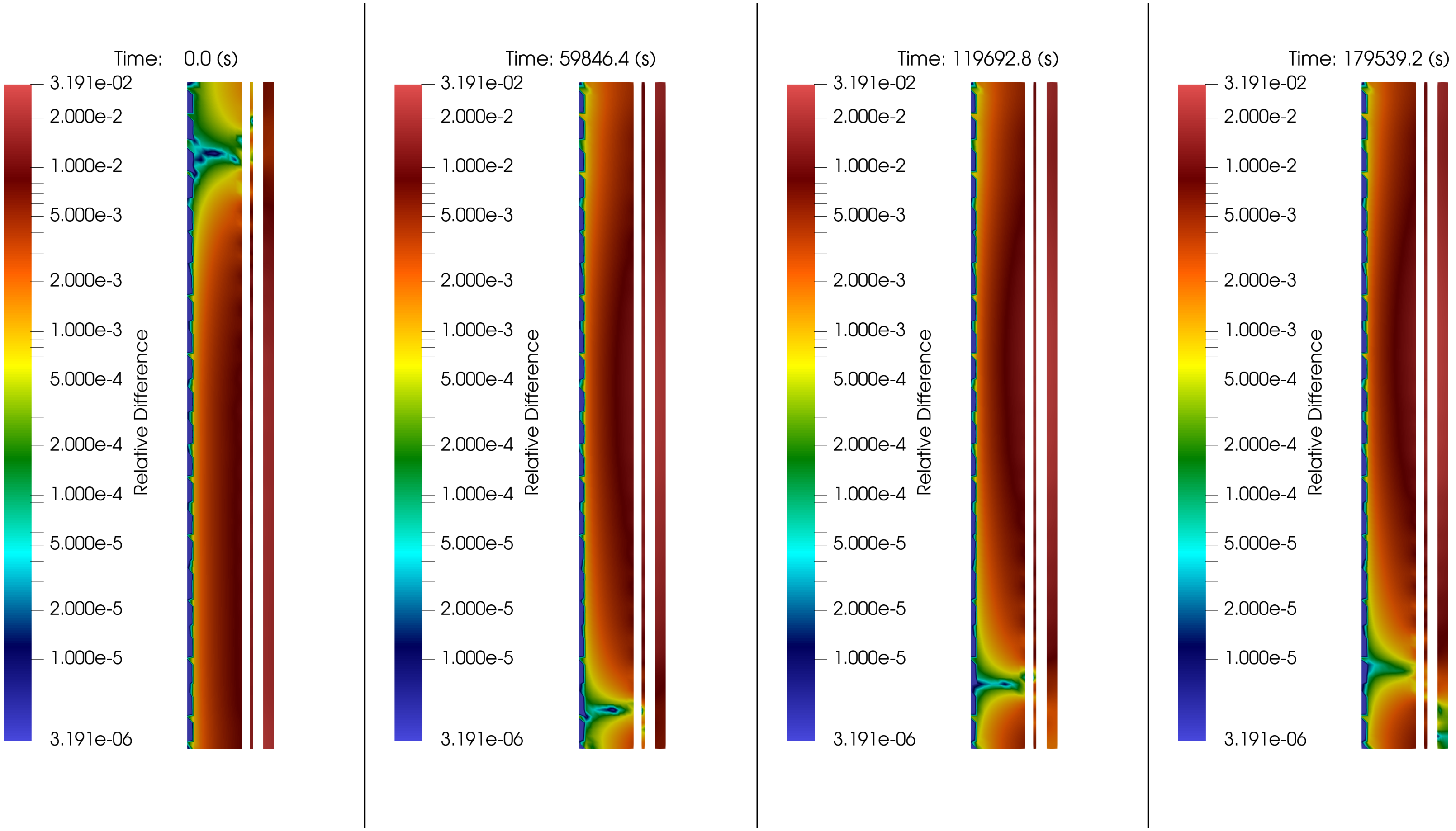

Figure 11: Comparison of 3D net radiation method and 2D R-Z thermal resistance method.

4. NEUTRON PRECURSOR DRIFT

Open-pool-type MSR concepts are liquid-fueled reactor designs where fissionable isotopes are dissolved in either fluoride or chloride molten salts. The modeling of these Molten Salt Reactor (MSR) concepts requires the inclusion of delayed neutron precursor (DNP) advection to account for the decay of DNPs across the core. The basic theory and kernel description from the Griffin [15] application is included in Section 4.1. In Section 4.2, we describe the test model of the molten-salt fast reactor design [16]. Finally, the results from the steady-state simulation are presented in Section 4.3.

4.1 Methodology

In open-pool-type MSR concepts, the DNP equations include an advection term

$$\frac{\partial}{\partial t}C_i + \vec{\nabla} \cdot (\vec{u}C_i) + \lambda_i C_i = \beta_i \sum_{g'=1}^{G} \nu\Sigma_{\mathrm{f},g'}\Phi_{g'}, \quad i = 1, \cdots, I, \tag{29}$$

where $\vec{u}$ is the bulk velocity of the liquid fuel, C_i is the concentration of the ith DNP group, λ_i is the decay constant for the ith DNP, β_i is the delayed neutron fraction for the ith DNP group and $\nu\Sigma_{\mathrm{f},g'}\Phi_{g'}$ is the total neutron production in group g'.

Typically, one assumes that the flow is incompressible, and thus, the velocity field satisfies the divergence-free form of the continuity equation

$$\vec{\nabla} \cdot \vec{u} = 0. \tag{30}$$

With the incompressibility approximation the DNP equation takes the form

$$\frac{\partial}{\partial t}C_i + \vec{u} \cdot \vec{\nabla}C_i + \lambda_i C_i = \beta_i \sum_{g'=1}^{G} \nu\Sigma_{\mathrm{f},g'}\Phi_{g'}, \quad i = 1, \cdots, I. \tag{31}$$

The solution to Equation 31 requires boundary conditions on the in-flow boundaries (i.e. $\partial\mathcal{D}_{\mathrm{in}} \equiv \{\vec{x} \in \partial\mathcal{D}, \vec{n}(\vec{x}) \cdot \vec{u} < 0\}$). Typically, we assume the perfect mixing of DNPs at the core outlet ($\partial\mathcal{D}_{\mathrm{out}} \equiv \{\vec{x} \in \partial\mathcal{D}, \vec{n}(\vec{x}) \cdot \vec{u} > 0\}$) before re-entering the core uniformly after a temporal delay outside of the active core,

$$C_i = \frac{e^{-\lambda_i \tau} \int_{\partial \mathcal{D}_{\text{out}}} |\vec{u} \cdot \vec{n}| C_i \, dx}{\int_{\partial \mathcal{D}_{\text{in}}} |\vec{u} \cdot \vec{n}| \, dx}, \tag{32}$$

where τ is the time that it takes the liquid fuel to flow from the outlet back into the inlet outside of the active core. Some MSR designs may have complicated inventory controls that can potentially extract or inject delayed neutron precursors from or into the primary system, respectively. In such cases, the boundary condition can be extended with a more sophisticated inventory control model.

In steady state, we cannot evaluate the DNPs algebraically as in the traditional equilibrium state, i.e.:

$$C_i = \frac{\beta_i}{\lambda_i} \sum_{g'=1}^{G} \nu \Sigma_{\text{f},g'} \Phi_{g'}, \quad i = 1, \cdots, I, \tag{33}$$

thus one cannot merge the prompt and delayed source terms in the neutron transport equation.

The DNP equations must be solved in conjunction with the multigroup neutron transport equation. We define the following advection operator:

$$\mathbb{T}_\text{c} \mathbf{C} \equiv \begin{bmatrix} \vec{u} \cdot \vec{\nabla} C_1 \\ \vec{u} \cdot \vec{\nabla} C_2 \\ \vdots \\ \vec{u} \cdot \vec{\nabla} C_I \end{bmatrix}.$$

The coupled equations can be written in operator notation

$$\frac{\partial}{\partial t} \left(\frac{\mathbf{\Psi}}{\mathbf{v}} \right) + \mathbb{L} \mathbf{\Psi} = \mathbf{Q}^{\text{ext}} + \mathbb{S} \mathbf{\Psi} + \mathbb{F}_\text{p} \mathbf{\Psi} + \mathbb{C} \mathbf{C}, \tag{34}$$

$$\frac{\partial}{\partial t} \mathbf{C} + \mathbb{T}_\text{c} \mathbf{C} + \boldsymbol{\lambda} \mathbf{C} = \mathbb{P} \mathbf{\Phi}, \tag{35}$$

where $\mathbf{\Psi}$ is the angular flux, $\mathbf{v}$ is the neutron velocity, $\mathbb{L}$ is the streaming and collision, $\mathbf{Q}^{\text{ext}}$ is the external source, $\mathbb{S}$ is the scattering source, $\mathbb{F}_\text{p}$ is the prompt neutron production, $\mathbb{C}$ is the multigroup delayed neutron production, and $\mathbb{P}$ is the delayed neutron production.

The typical boundary and initial conditions apply to the neutron transport equation along with the initial condition for the DNPs. The only difference is the introduction of the DNP advection term $\mathbb{T}_\mathrm{c}\mathbf{C}$ in the DNP equation and the in-flow boundary condition for $\mathbf{C}$ on $\partial\mathcal{D}_\mathrm{in}$:

$$\mathbf{C} = \mathbb{F}_\mathrm{c}\mathbf{C}, \tag{36}$$

where $\mathbb{F}_\mathrm{c}$ maps the DNP concentration from $\partial\mathcal{D}_\mathrm{out}$ to $\partial\mathcal{D}_\mathrm{in}$ and is defined as

$$\mathbb{F}_\mathrm{c}\mathbf{C} \equiv \frac{1}{\int_{\partial\mathcal{D}_\mathrm{in}} |\vec{u}\cdot\vec{n}|\,dx} \begin{bmatrix} e^{-\lambda_1\tau}\int_{\partial\mathcal{D}_\mathrm{out}} |\vec{u}\cdot\vec{n}|C_1\,dx \\ e^{-\lambda_2\tau}\int_{\partial\mathcal{D}_\mathrm{out}} |\vec{u}\cdot\vec{n}|C_2\,dx \\ \vdots \\ e^{-\lambda_I\tau}\int_{\partial\mathcal{D}_\mathrm{out}} |\vec{u}\cdot\vec{n}|C_I\,dx \end{bmatrix}.$$

The steady-state equation is

$$\mathbb{L}\mathbf{\Psi} = \mathbf{Q}^\mathrm{ext} + \mathbb{S}\mathbf{\Psi} + \mathbb{F}_\mathrm{p}\mathbf{\Psi} + \mathbb{C}\mathbf{C}, \tag{37}$$

$$\mathbb{T}_\mathrm{c}\mathbf{C} + \boldsymbol{\lambda}\mathbf{C} = \mathbb{P}\mathbf{\Phi}. \tag{38}$$

The k-eigenvalue problem is

$$\mathbb{L}\mathbf{\Psi} = \mathbb{S}\mathbf{\Psi} + \frac{1}{k}\mathbb{F}_\mathrm{p}\mathbf{\Psi} + \mathbb{C}\mathbf{C}, \tag{39}$$

$$\mathbb{T}_\mathrm{c}\mathbf{C} + \boldsymbol{\lambda}\mathbf{C} = \frac{1}{k}\mathbb{P}\mathbf{\Phi}. \tag{40}$$

Similarly, we can obtain the neutron diffusion equation with DNP convection. An adjoint equation can be derived. We emphasize that the DNP equations cannot be merged into the neutron transport equation and must be solved separately, even in steady-state

4.2 Problem Description

The test problem is based on the Molten Salt Fast Reactor (MSFR) design [16]. An illustration of the design is shown in Figure 12. The MSFR is a fast-spectrum reactor that uses a fluoride-based fuel salt with a thorium fuel cycle. The main specifications are shown in Table 7, and the material properties are from [16]. The modeled geometry is modified from the original rectangular geometry and replaced with curved surfaces similar to those in "Geometry II" from [17]. The computational model is derived from [18], where the cross sections were prepared with a Serpent 2 model of the core in six coarse energy groups.

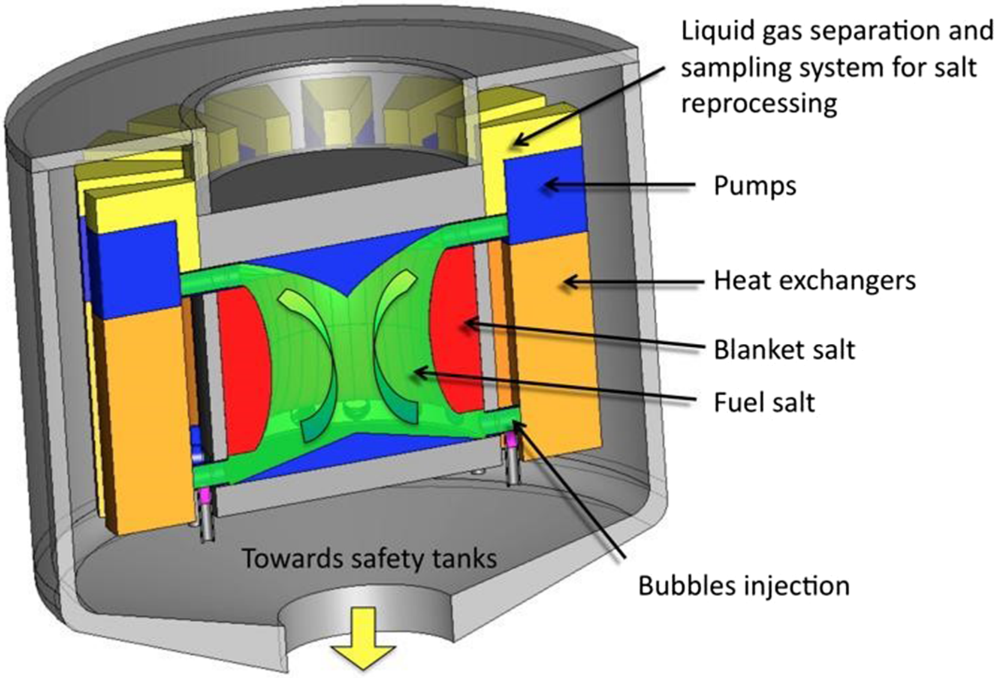

Figure 12: Conceptual design of the MSFR [3].

Table 7: Specifications for the MSFR.

Parameter	Value
Rated power	3000 MWth
Core inlet/outlet temperature	923/1023 K
Flow rate	4.5 m^3/s
Salt volume	18 m^3
Salt composition	LiF-ThF$_4$-(^{233}U/TRU)F$_4$
Core height	2.255 m
Core diameter	2.255 m

The computational model includes a core region, pump, and a heat exchanger. The following assumptions and simplifications are made:

- The blanket salt region is ignored in both neutronics and thermal fluids.
- Conjugate heat transfer between structures or components and the salt is ignored, except in the heat exchanger.
- The pump is modeled as a momentum source term for the y-component of the velocity variable with a value of 2.0E4 $kg/m^2/s^2$.
- The friction coefficient is adjusted to 5.e3 in order to obtain the correct mass flow rate and the approximate pressure drop in the heat exchanger.
- The heat exchanger is modeled using a heat sink kernel with a surface area density of 600 m^2/m^3, a heat transfer coefficient of 20 $kW/m^2/K$, and an ambient temperature of 600^oC.
- A mixing length model is used, available from the MOOSE framework.
- The Boussinesq buoyancy model is used to account for buoyant forces within the fluid.

Two mesh files were developed for 2D and 3D axisymmetric models and are shown in Figure 13. In this report, we seek to present the results for the steady-state case. The purpose of the 3D model is to test the consistency of the solvers with a more realistic geometry. The solution for the MSFR is obtained by tightly coupling Griffin and Pronghorn via a Picard iteration scheme. Griffin solves Equation 39 using the diffusion approximation with CFEM dicretization, while Pronghorn solves the incompressible flow equations discretized using the FVM. The spatial concentrations of the neutron precursor groups are obtained from the solution to the passive scalar decay-transmutation-advection equations in Equation 40. The flow model used is known as a mixing length model. This assumes that the reynolds stress tensor takes a form that only involves the time-averaged flow and an additional unknown called the eddy viscosity [19]. This eddy viscosity is handled with what are known as turbulence closure models. The standard for turbulence closure models are typically two equation models. The most common are the k-epsilon and k-omega models and their derivatives. The model used here assumes the kinetic energy term in the Reynolds stress tensor approximation is negligible and results in the eddy viscosity being the only unknown to be solved. The eddy viscosity closure is known as an algebraic model, specifically a mixing length model. The mixing length model correlates eddy viscosity to a mixing length squared and the magnitude of the wall shear stress as is shown in [19]. The mixing length is then approximated as a constant multiplied by the distance to the nearest boundary. This constant is frequently referred to as the Von Karman constant and has been determined experimentally.

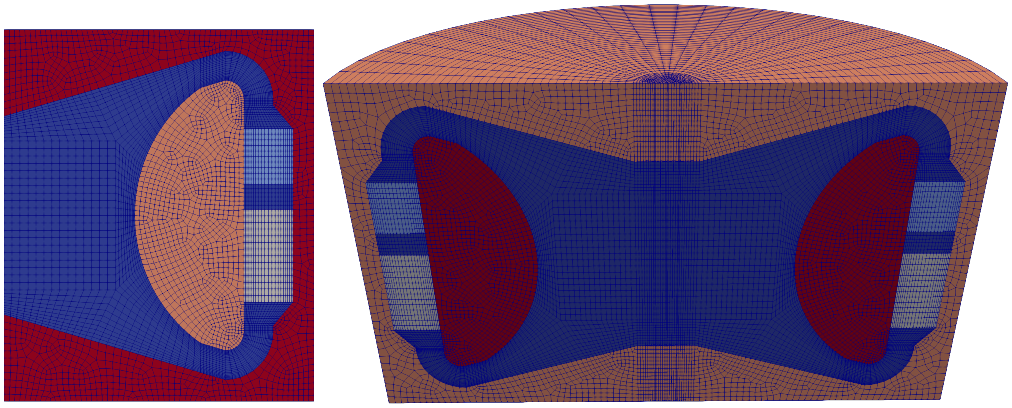
(a) 2D axisymmetric (b) 3D axisymmetric

Figure 13: Computational mesh for the Griffin and Pronghorn models.

4.3 Results and Discussion

The results from the 2D steady-state simulation are shown in Figure 14. The fission source peak occurs in the center of the symmetry of the active core, since there is no fertile blanket. The highest fuel temperatures occur at the top of the active core near the reflector. The velocity field looks good for the primitive model that we used. With one and two equation models, small recirculation zones may be expected to appear in the top center and bottom center of the core region, but this will depend on flow rates and local velocities. Only a moderate boundary separation occurs in the pump region. The pump is merely modeled as a momentum source, so this is not the exact geometry. This does give us a good evaluation of how the precursors are advected through the core and what effect this may have on the kinetics. The temperature is as expected with a top peaked temperature profile in the center of the core. With recirculation, the temperature profile may not peak as much at the top due to the increased mixing, but this will depend on the exact local flow conditions. This isn't a simple geometry, and as a result, making predictions of how more accurate models will behave is difficult. Negative pressures can be seen in the plot, but negative pressures are expected. With an incompressible flow, the pressure becomes relative, and a fixed point is needed to get a unique solution for pressure. In this simulation, the fluid properties are considered constant, so the fixed point is arbitrary. MOOSE handles this in a unique way where, instead of setting a single cell or node to a specific value, it uses a Lagrange multiplier to ensure that the average of the field is equal to a set average, zero in this case. This provides the necessary constraint for a unique pressure solution.

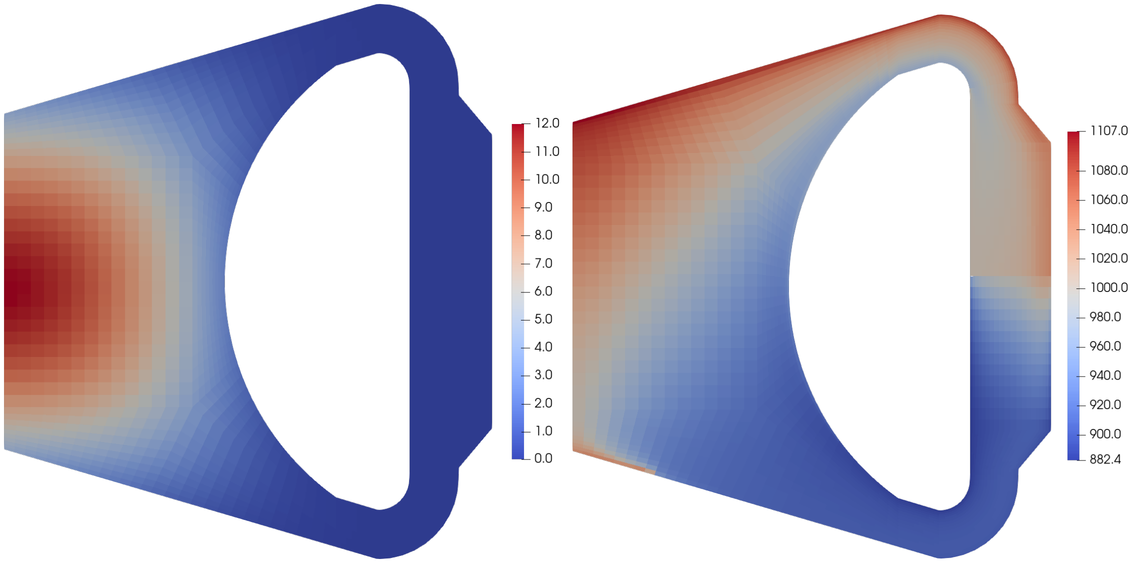

(a) Fission source (scaled) (b) Temperature [K]

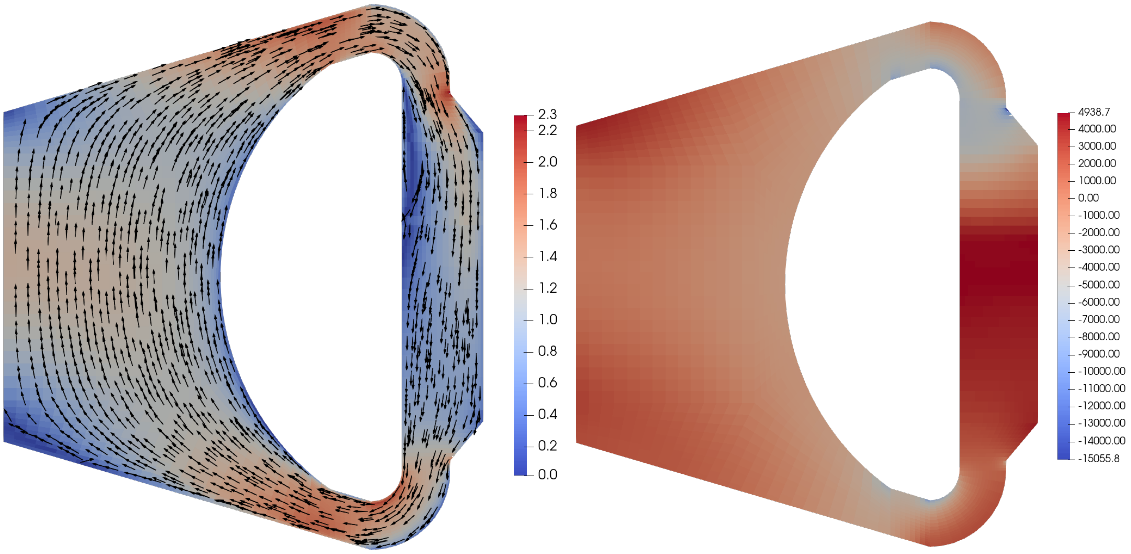

(c) Velocity [m/s] (d) Pressue [Pa]

Figure 14: Steady-state solution for the MSFR.

Figure 15 shows the spatial distribution delayed neutron precursor concentrations for Delayed Groups 1, 3, and 6 half-lives of 52.1, 6.02, and 0.238 seconds, respectively. The concentrations are normalized to unity. In Delayed Neutron Groups 1 and 3, the half-life is of the same or larger order than the fluids time constant (salt volume/flow rate), and this leads to solutions that show significant advection by the fluid. The half-life in Group 6 is much smaller than the fluids time constant, thus it dominates the spatial distribution and yields a solution that resembles the fission source. The pressure distribution shows a total range of 20 kPa, which is consistent with prior work showing pressure drops around 10 kPa for a similar configuration [20]. The assumptions, models, and detail can account for the differences between the results.

In the future, it will be desirable to use turbulence models that align better with industry standards. A simple one equation model will likely be more revealing, and a two equation model will align the analysis with current turbulence modeling standards. This is especially true when looking at the constants that would become less tunable parameters and instead experimentally verified constants. Transient analysis is another item that needs to be investigated. The precursor distributions are going to be affected by flow rates, and as a result, the effective delayed neutron fraction will as well. 3D simulations would also need to be investigated, which was attempted here, but there were substantial issues encountered when simulating a 3D core.

For the 3D model, we encountered the following problems:

- The run time was very slow and impractical for the geometry created.
- The run time was accompanied by very high memory usage, which made it impractical for use in design evaluations.

Further development should resolve both these issues. The very slow run time is partially due to coupling the precursor equations within the thermal-hydraulics solve. Because the distribution of the precursors has no effect on the fluid flow, the two equation sets should be separated. This will considerably reduce the size of the non-linear equation system, limiting the computational cost and, in some capacity, the memory cost. In order to achieve this, we need to rework the advection kernels to be able to detect flow boundary conditions for an auxiliary velocity variable. This auxiliary variable is transferred from the fluid flow simulation to the precursor advection solve. Improved numerical techniques are required to apply this MOOSE functionality to large problems as the main problem for solve speed is within the navier stokes system.

The high memory usage is currently due to caching the face variables and gradients on the cell faces. In the finite volume method, the pressure gradient and velocities have to be evaluated on cell faces rather at a quadrature point. This evaluation can be expensive, depending on the numerical scheme used. For example, at the boundaries of the domain, the implementation of the Rhie Chow interpolation in [21] requires both the face values and the gradient, which itself depends on the face value. Because we do not lag any quantity, unlike in segregated solvers, we have to solve a linear system to obtain both quantities. Due to this expected cost, we cached face variables and gradients. Recent profiling has shown that the cost was initially overestimated and that caching is not necessary for performance. The memory cost is reduced by up to 70% with this upcoming change.

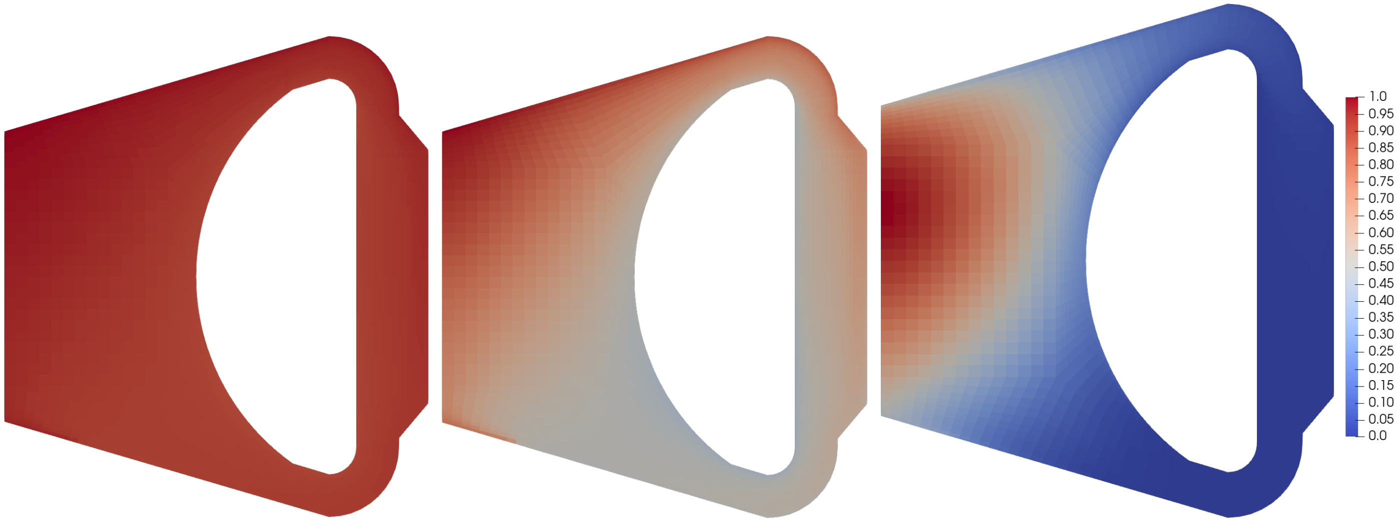

(a) Group 1

(b) Group 3

(c) Group 6

Figure 15: Spatial distribution of the precursor group concentrations (normalized to unity).

5. 2D-1D THERMAL HYDRAULICS COUPLING

This chapter is focused on the implementation of the multiphysics coupling acceleration in MOOSE. The acceleration methods were implemented in the context of Deliverable 8g to enable the coupling of coarse mesh multidimensional solvers and 1D balance of plant simulations. We detail the context of this work in Subsection 5.1, and then in Section 5.2, we describe the additional methods implemented in the MOOSE framework to accelerate multiphysics coupling iterations. Later, we present results in Subsection 5.3 for their application to the 3D-1D coupling of thermal hydraulics solvers. Finally, we present in Subsection 5.4 additional methods that may be implemented in the MOOSE framework to deliver even faster multiphysics coupling acceleration.

5.1 Context

For intermediate-fidelity nuclear reactor simulations, we plan to combine a 3D (or 2D-RZ) multiphysics solve of the core region with a 1D model of the heat transfer loops. This multidimensional approach is used to balance computational costs and benefits. The 3D representation of the core is able to more closely examine potential limiting factors in the core, such as a high fuel temperature, than a 1D approach of the core. A 1D approach would require high conservatism for estimating failure limits. On the other hand, a 1D model for the rest of the heat transfer loops can coarsely and cheaply model these large regions, and while these regions also play a large role in the safety analysis of nuclear reactors, a detailed local multidimensional approach is only beneficial for a narrow selection of accidental transients.

The major difficulty in this approach is the coupling between the two thermal hydraulics solves. In order to couple the core model to the 1D loops, we exchange pressure, velocity, and temperature at both the inlet and outlet of the core. The 3D core solver receives the core inlet velocity and temperature and the core outlet pressure from the 1D solver, while the 1D solver receives the core outlet velocities and the temperature and core inlet pressure from the 3D core solver. Those quantities are coupled, in that the quantities computed at the core outlet strongly depend on the core inlet, and similarly, the core inlet temperature and velocity/mass flow rate also depend on the core outlet conditions. Because of this coupling, we have to iterate between the two solves to converge the core inlet and outlet conditions. This coupling can be quite difficult, as the exchange of pressure boundary conditions causes pressure waves propagating through each domain. Changes in pressure boundary conditions may cause changes in material properties, especially for compressible flow, and prevent the rapid generation of a new numerical solution from the previous iteration solution.

In a first implementation of this coupling by researchers at Argonne National Laboratory, this coupling was performed using the native MOOSE capabilities for Picard iterations. They found that convergence was both slow and unreliable in that the coupling could diverge. In order to resolve this latter issue, the coupling was under-relaxed. The values transferred from the 1D solver to the 3D (or 2D in this case) solver for the boundary conditions were blended using a constant relaxation factor with the values from the previous iteration. This stabilized the coupling but further slowed it down, sometimes requiring more than 100 iterations of running both solvers to sufficiently converge a single timestep. The number of iterations was artificially capped at 10 in order to limit the computational expense, at the detriment of the fidelity of the results.

5.2 Multiphysics Coupling Acceleration Methods

We implemented two simple fixed point algorithms, the secant method and Steffensen's [22] method, to demonstrate the potential for advanced multiphysics tight coupling acceleration. We refer to as tight coupling as an iterative process between two physics solved separately, with information passed after the completion of each solve. The process is continued until mutual convergence is achieved.

5.2.1 Secant method

The secant method is a root finding technique that follows secant lines to find the roots of a function f. It is adapted here for fixed point iterations. The secant method may be described by the following equation:

$$x_{n+1} = x_n - \frac{(f(x_n) - x_n) \cdot (x_n - x_{n-1})}{f(x_n) - x_n - f(x_{n-1}) + x_{n-1}}. \tag{41}$$

where x_n is the specified variable/postprocessor and f is a function representing the coupled multiphysics problem. A relaxation factor may be added to the method, though it will reduce the order of convergence. The secant method is easily understood for 1D problems, where $(x_n, f(x_n) - x_n)$ are the coordinates of the points used to draw the secant, of slope:

$$\frac{x_n - x_{n-1}}{(f(x_n) - x_n) - (f(x_{n-1}) - x_{n-1})}. \tag{42}$$

The convergence of the secant method is expected to be super-linear with an order of $\frac{1+\sqrt{5}}{2}$. However convergence is not guaranteed. Some conditions for convergence at this convergence rate is that the equations are twice differentiable in their inputs, with a fixed point multiplicity of one. Oscillatory functions and poor initial guesses can prevent convergence.

5.2.2 Steffensen's method

Steffensen's method is a root finding technique based on perturbating a solution at a given point to approximate the local derivative, such that:

$$g(x_n) = \frac{f(x_n + f(x_n))}{f(x_n)} \tag{43}$$

$$x_{n+1} = x_n - \frac{f(x_n)}{g(x_n)}. \tag{44}$$

The update is then similar to Newton's method, which uses the exact derivative. The convergence of Steffensen's method is expected to be quadratic. However, because it requires two evaluations of the coupled problem before computing the next term, this method is expected to be slower than the secant method. A poor initial guess can also prevent convergence.

5.3 Results

We applied these methods to a coupling problem using the SAM [23] code developed at Argonne National Laboratory. A 2D-RZ core thermal hydraulics simulation of a fluoride-salt-cooled pebble-bed high-temperature reactor is coupled to a 1D model of the rest of the primary loop and the secondary loop. The coupling is performed by exchanging boundary conditions between the two codes, using the primitive variables of pressure, temperature, and velocity. Conservation of mass, momentum, and energy at the interface is improved by using the same equation of state in both codes, though additional care is usually necessary with the finite element discretization of the equations. We summarize this problem in Figure 16.

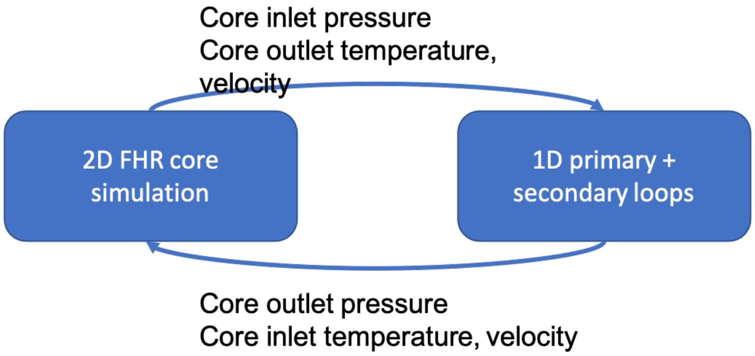

Figure 16: Sketch of the 2D-1D coupling problem.

We examine the number of iterations necessary to complete the tight coupling of the two solves for the first 20 time steps of a relaxation transient in Figure 17. The number of iterations to converge the coupling is initially very large, as both solves start with a poor constant initialization. As the relaxation pseudo-transient progresses, the number of iterations to converge the coupling reduces, and we would expect it to reach zero at convergence. Throughout the whole transient, both the secant method and Steffensen's method outperform Picard iterations significantly, with between 3× and 6× fewer iterations. The effect of relaxation on Picard's method is very significant, doubling the number of iterations necessary for convergence.

5.4 Potential for Future Work

The methods that were implemented for this work are relatively simple and do not truly achieve quadratic convergence. We limited our scope to these methods because their implementation already required a significant rework of the executioner system and the multiapps coupling system in MOOSE. With the rework now achieved, we may consider three classes of methods to achieve quadratic or higher convergence: the Newton method, additional quasi-Newton methods, and Shanks methods and their derivatives.

The Newton method is well known in the science and engineering community and needs no introduction. It is commonly used in MOOSE for individual solves, especially when using automatic differentiation [24] as this allows for the generation of ”perfect” Jacobians. This method

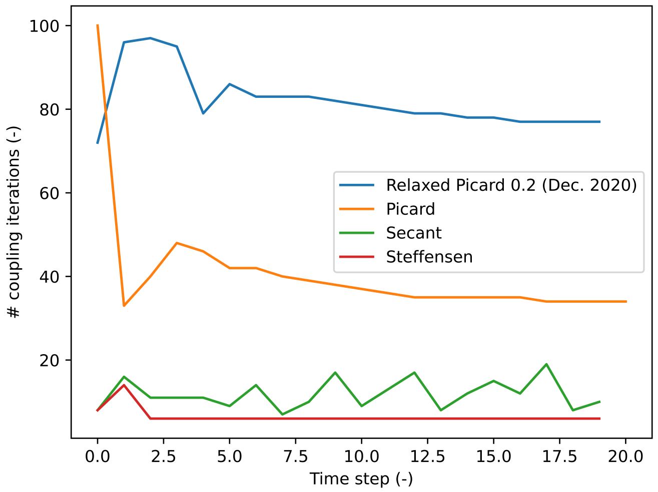

Figure 17: Iteration counts with various multiphysics coupling algorithms for a 2D-1D thermal hydraulics coupling problem.

could be used for multiphysics iterations with significant development in MOOSE. The automatic differentiation system can be extended to the auxiliary variables involved in the coupling. Then we could obtain the derivatives of the primary variables with regards to the auxiliary variables, in both applications, allowing to compute the Jacobian of the multiphysics problem. With this information, we could update the non-linear variables based on the change in the coupled quantities using Newton's method.

Quasi-Newton methods are based on approximating the Jacobian in the Newton method. The secant method and Steffensen's method can both be considered quasi-Newton methods. There are however many other quasi-Newton methods, and some, for example Broyden's method [25], can achieve quadratic convergence. This class of methods has been applied to multiphysics iteration problem [26, 27]. The implementation of these other methods can be performed with minimal development effort in the MOOSE framework. However, it is likely that they will only apply to the same categories of problems as the secant and Steffensen's method already apply to, albeit with an increased convergence order.

Finally, the Shanks transformation [28] is based on repeatedly applying the Aitken delta-squared transformation. It is related in that manner to Steffensen's method. It is classified as a non-linear sequence transformation. The acceleration provided by the Shanks transformation depends on the sequence accelerated. Its implementation in MOOSE would only require moderate development efforts, mostly to limit the memory cost of storing numerous vectors from several transforms of the variables. Related development of another method by Wynn, the epsilon algorithm [29], simplifies the application of the transformation and may be considered as well.

6. CONCLUSIONS

This report details the progress and activities of INL for the NRC project "Development and Modeling Support for Advanced Non-Light Water Reactors," for which we report the successful completion of one task. In addition, the extended-scope tasks have also been completed. The following deliverable completions are reported:

- Deliverable 1c: the implementation of the gas-mixture relations in Pronghorn was described. A problem mimicking the conditions achieved in a DLOFC event was solved with both RELAP-5 and Pronghorn. The comparison between the mass fraction spatial profiles computed with RELAP-5 and Pronghorn clearly shows the presence of numerical artifacts, (i.e., artificial diffusion) when the Kurganov-Tadmor (KT) discretization scheme is applied to the advection term. This is a known issue of the KT scheme when applied to low-Mach number and weakly compressible flows [9]. To solve this issue, future work will need to focus on the implementation of a robust solver with a weakly compressible formulation and the use of the PIMPLE algorithm [30]. A further improvement of the results can be achieved by implementing the air properties as real fluid rather than an ideal gas by leveraging References [31, 32]. Finally, the mixing model could be generalized by dropping the hypothesis of ideality of the gas mixture and allowing non-constant specific heat capacity.
- Deliverable 2a: we demonstrate two approaches to model the radiation/conduction/natural convection heat transfer across a stagnant gas for the PBMR-400 design using Pronghorn. The first approach is based on the net radiation method, which relies on the computation of view factors with the MOOSE ray tracing capability. The second method is a traditional thermal resistance approach. The test problems include both 2D and 3D geometries. In all cases, the results show very good agreement with maximum differences within 3.2 K during a DLOFC transient. This confirms that the faster thermal resistance method produces solutions that are equivalent to the net radiation method for this geometry.
- Deliverable 3d: we demonstrated the use of the advection kernel for the delayed neutron precursor equation in Griffin with a 2D MSFR model. The results appear physical but further verification is recommended. We also recommend the addition of a conjugate heat transfer

to compute the temperatures and model the thermomechanic behavior of the reflectors and other structures. In addition, we attempted to build and execute a 3D axisymmetric model, but experienced difficulties with the memory usage and runtime performance. Further investigation is necessary to determine the source of these issues.

- Deliverable 8g: we implemented a faster multiphysics iteration coupling algorithm, which provided overall a 6× acceleration of the 3D-1D coupling of the core multidimensional fluid flow solver and the 1D primary and secondary loop model. These methods are generally applicable to any multiphysics problem in which the solves are separated with different matrices, which is also called tight coupling. The necessary rework of the executioner system and the multiapp coupling in MOOSE opens future options for state-of-the-art fixed point algorithms at a moderate development cost.

REFERENCES

[1] P. Williams, F. Silady, T. Dunn, R. Noren, D. McEachern, D. Dilling, J. Berkoe, F. Homan, L. Mears, S. Penfield Jr, *et al.*, "MHTGR development in the United States," *Progress in Nuclear Energy*, vol. 28, no. 3, pp. 265–346, 1994.

[2] N. E. Agency, "Benchmark of the modular high-temperature gas-cooled reactor 350 mw core design," Tech. Rep. NEA/NSC/R(2017)4, Organization for Economic Co-operation and Development, 2 2018.

[3] M. Allibert, M. Aufiero, M. Brovchenko, S. Delpech, V. Ghetta, D. Heuer, A. Laureau, and E. Merle-Lucotte, *Handbook of Generation IV Nuclear Reactors*. edited by I. Pioro, Woodhead Publishing Series in Energy (Woodhead Publishing, Duxford, UK), 2015.

[4] A. Novak, R. Carlsen, S. Schunert, P. Balestra, R. Slaybaugh, and R. Martineau, "Pronghorn: A multidimensional coarse mesh application for advanced reactor thermal-hydraulics," *submitted to Nucl. Techn.*, 2021.

[5] C. R. Wilke, "A viscosity equation for gas mixtures," *Journal Chem Physics*, vol. 18, pp. 517–519, 1950.

[6] RELAP5 Development Team, "Relap5/mod3 code manual, code structure, system models, and solution methods," Tech. Rep. INEL-95/0174, INL, 7 1995.

[7] E. A. Mason and S. C. Saxena, "Approximate formula for the thermal conductivity of gas mixtures," *Journal Chem Physics*, vol. 1, pp. 361–369, 1958.

[8] Idaho National Laboratory, "MOOSE multiphysics object-oriented simulation environment." https://www.mooseframework.org, 2018.

[9] A. Kurganov and E. Tadmor, "New high-resolution central schemes for nonlinear conservation laws and convection–diffusion equations," *Journal of Computational Physics*, vol. 160, no. 1, pp. 241–282, 2000.

[10] C. D. Laney, *Computational Gasdynamics*. Cambridge University Press, 1998.

[11] RELAP5 Development Team, "RELAP5-3D Code Manual Volume I: Code Structure, System Models and Solution Methods," Tech. Rep. INL/MIS-15-36723, Revision 4.4, Idaho National Laboratory, 2018.

[12] E. W. Lemmon, M. O. McLinden, and D. G. Friend, *Thermophysical Properties of Fluid Systems*. NIST Chemistry WebBook, NIST Standard Reference Database Number 69, Eds. P.J. Linstrom and W.G. Mallard, National Institute of Standards and Technology, June 24, 2021.

[13] OECD/NEA, "PBMR Coupled Neutronics/Thermal-hydraulics Transient Benchmark The PBMR-400 Core Design," Tech. Rep. NEA/NSC/DOC(2013)10, OECD/NEA, July 2013.

[14] Balestra, Paolo, Schunert, Sebastian, Carlsen, Robert W, Novak, April J, DeHart, Mark D, and Martineau, Richard C, "PBMR-400 benchmark solution of exercise 1 and 2 using the moose based applications: MAMMOTH, Pronghorn," *EPJ Web Conf.*, vol. 247, p. 06020, 2021.

[15] Y. Wang, S. Schunert, J. Ortensi, V. Laboure, M. DeHart, Z. Prince, F. Kong, J. Harter, P. Balestra, and F. Gleicher, "Rattlesnake: A moose-based multiphysics multischeme radiation transport application," *Nuclear Technology*, vol. 207, no. 7, pp. 1047–1072, 2021.

[16] Brovchenko, Mariya, Kloosterman, Jan-Leen, Luzzi, Lelio, Merle, Elsa, Heuer, Daniel, Laureau, Axel, Feynberg, Olga, Ignatiev, Victor, Aufiero, Manuele, Cammi, Antonio, Fiorina, Carlo, Alcaro, Fabio, Dulla, Sandra, Ravetto, Piero, Frima, Lodewijk, Lathouwers, Danny, and Merk, Bruno, "Neutronic benchmark of the molten salt fast reactor in the frame of the evol and mars collaborative projects," *EPJ Nuclear Sci. Technol.*, vol. 5, p. 2, 2019.

[17] H. Rouch, O. Geoffroy, P. Rubiolo, A. Laureau, M. Brovchenko, D. Heuer, and E. Merle-Lucotte, "Preliminary thermal–hydraulic core design of the molten salt fast reactor (msfr)," *Annals of Nuclear Energy*, vol. 64, pp. 449–456, 2014.

[18] A. Abou-Jaoude, S. Harper, G. Giudicelli, P. Balestra, S. Schunert, N. Martin, A. Lindsay, and M. Tano, "A workflow leveraging moose transient multiphysics simulations to evaluate the impact of thermophysical property uncertainties on molten-salt reactors," *Annals of Nuclear Energy (Preprint submitted)*, 2021.

[19] Idaho National Laboratory, "MOOSE multiphysics object-oriented simulation environment." https://mooseframework.inl.gov/modules/navier_stokes/rans_theory.html, 2018.

[20] H. Rouch, O. Geoffroy, P. Rubiolo, A. Laureau, M. Brovchenko, D. Heuer, and E. Merle-Lucotte, "Preliminary thermal–hydraulic core design of the molten salt fast reactor (msfr)," *Annals of Nuclear Energy*, vol. 64, pp. 449–456, 2014.

[21] F. Moukalled, L. Mangani, and M. Darwish, *The Finite Volume Method in Computational Fluid Dynamics*. Springer, 2015.

[22] L. W. Johnson and D. R. Scholz, "On Steffensen's Method," *SIAM Journal on Numerical Analysis*, vol. 5, pp. 296–302, 1968.

[23] R. Hu, "SAM theory manual," Tech. Rep. ANL/NE-17/4, Argonne National Laboratory, 2017.

[24] A. Lindsay, R. Stogner, D. Gaston, D. Schwen, C. Matthews, W. Jiang, L. K. Aagesen, R. Carlsen, F. Kong, A. Slaughter, C. Permann, and R. Martineau, "Automatic differentiation in metaphysicl and its applications in moose," *Nuclear Technology*, vol. 207, no. 7, pp. 905–922, 2021.

[25] C. G. Broyden, "A class of methods for solving nonlinear simultaneous equations," *Math. Comp.*, vol. 19, pp. 577–593, 1965.

[26] R. Haelterman, D. Van Eester, and D. Verleyen, "Accelerating the solution of a physics model inside a tokamak using the (inverse) column updating method," *Journal of Computational and Applied Mathematics*, vol. 279, pp. 133–144, 2015.

[27] I. Ramière and T. Helfer, "Iterative residual-based vector methods to accelerate fixed point iterations," *Computers & Mathematics with Applications*, vol. 70, no. 9, pp. 2210–2226, 2015.

[28] D. Shanks, "Non-linear transformations of divergent and slowly convergent sequences," *Journal of Mathematics and Physics*, vol. 34, no. 1-4, pp. 1–42, 1955.

[29] P. Wynn, "Acceleration Techniques in Numerical Analysis, with Particular Reference to Problems in One Independent Variable," *Proc. IFIPS, Munich.*, pp. 149–156, 1962.

[30] “Openfoam guide/the pimple algorithm in openfoam.” `https://openfoamwiki.net/index.php/OpenFOAM_guide/The_PIMPLE_algorithm_in_OpenFOAM`, note = Accessed: 2021-06-30.

[31] E. W. Lemmon, R. Jacobsen, S. G. Penoncello, and D. G. Friend, “Thermodynamic properties of air and mixtures of nitrogen, argon, and oxygen from 60 to 2000 k at pressures to 2000 mpa,” *Journal of Physical and Chemical Reference Data*, vol. 29, pp. 331–385, 2000.

[32] E. W. Lemmon and R. T. Jacobsen, “Viscosity and thermal conductivity equations for nitrogen, oxygen, argon, and air,” *International Journal of Thermophysics*, vol. 25, pp. 21–69, 2004.